ALMA [N II] 205 μm Imaging Spectroscopy of the Interacting Galaxy System BRI 1202-0725 at Redshift 4.7[*]

Nanyao Lu[1,2], Yinghe Zhao[3,4,5], Tanio Díaz-Santos[6], C. Kevin Xu[1,2], Vassilis Charmandaris[7,8], Yu Gao[9], Paul P. van der Werf[10], George C. Privon[11,12], Hanae Inami[13], Dimitra Rigopoulou[14], David B. Sanders[15], and Lei Zhu[1,2]

[1] National Astronomical Observatories, Chinese Academy of Sciences (CAS), Beijing 100012, China; nanyao.lu@gmail.com
[2] China-Chile Joint Center for Astronomy, Camino El Observatorio 1515, Las Condes, Santiago, Chile
[3] Yunnan Observatories, Chinese Academy of Sciences, Kunming 650011, China
[4] Key Laboratory for the Structure and Evolution of Celestial Objects, Chinese Academy of Sciences, Kunming 650011, China
[5] Center for Astronomical Mega-Science, CAS, 20A Datun Road, Chaoyang District, Beijing 100012, China
[6] Nucleo de Astronomia de la Facultad de Ingenieria, Universidad Diego Portales, Av. Ejercito Libertador 441, Santiago, Chile
[7] Department of Physics, University of Crete, GR-71003 Heraklion, Greece
[8] IAASARS, National Observatory of Athens, GR-15236, Penteli, Greece
[9] Purple Mountain Observatory, CAS, Nanjing 210008, China
[10] Leiden Observatory, Leiden University, P.O. Box 9513, 2300 RA Leiden, The Netherlands
[11] Departamento de Astronomía, Universidad de Concepción, Casilla 160-C, Concepción, Chile
[12] Pontificia Universidad Católica de Chile, Instituto de Astrofísica, Casilla 306, Santiago 22, Chile
[13] Centre de Recherche Astrophysique de Lyon (CRAL), Observatoire de Lyon, CNRS, UMR5574, F-69230, Saint-Genis-Laval, France
[14] Department of Physics, University of Oxford, Keble Road, Oxford OX1 3RH, UK
[15] University of Hawaii, Institute for Astronomy, 2680 Woodlawn Drive, Honolulu, HI 96822, USA

Abstract

We present the results from Atacama Large Millimeter/submillimeter Array imaging in the [N II] 205 μm fine-structure line (hereafter [N II]) and the underlying continuum of BRI 1202-0725, an interacting galaxy system at $z = 4.7$, consisting of a quasi-stellar object (QSO), a submillimeter galaxy (SMG), and two Lyα emitters, all within ~25 kpc of the QSO. We detect the QSO and SMG in both [N II] and continuum. At the ~1″ (or 6.6 kpc) resolution, both the QSO and SMG are resolved in [N II], with the de-convolved major axes of ~9 and ~14 kpc, respectively. In contrast, their continuum emissions are much more compact and unresolved even at an enhanced resolution of ~0″.7. The ratio of the [N II] flux to the existing CO(7−6) flux is used to constrain the dust temperature (T_{dust}) for a more accurate determination of the FIR luminosity L_{FIR}. Our best estimated T_{dust} equals 43 (±2) K for both galaxies (assuming an emissivity index $\beta = 1.8$). The resulting $L_{CO(7-6)}/L_{FIR}$ ratios are statistically consistent with that of local luminous infrared galaxies, confirming that $L_{CO(7-6)}$ traces the star formation (SF) rate (SFR) in these galaxies. We estimate that the ongoing SF of the QSO (SMG) has an SFR of 5.1 (6.9) × $10^3 M_\odot$ yr^{-1} (±30%) assuming Chabrier initial mass function, takes place within a diameter (at half maximum) of 1.3 (1.5) kpc, and will consume the existing 5 (5) × $10^{11} M_\odot$ of molecular gas in 10 (7) × 10^7 years.

Key words: galaxies: active – galaxies: ISM – galaxies: star formation – infrared: galaxies – ISM: molecules – submillimeter: galaxies

1. Introduction

Star formation rate (SFR) measures the fundamental physical process of transforming gas into stars and is one of the most important drivers of galaxy evolution. For high-z galaxies, Lu et al. (2015, hereafter Lu15) explored a new dual-spectral line approach for estimating *both* SFR and the far-infrared (FIR) color $C(60/100)$ (thus, T_{dust}), where $C(60/100)$ refers to the rest-frame $f_\nu(60\,\mu m)/f_\nu(100\,\mu m)$ ratio. For local (ultra-)luminous infrared galaxies ((U)LIRGs), the luminosity of the CO(7−6) line emission, $L_{CO(7-6)}$, can be used to infer the SFR of the galaxy with a ~30% accuracy, irrespective of whether the galaxy hosts an active galactic nucleus (AGN; Lu et al. 2014, 2017; Lu15). Furthermore, by measuring the flux of the [N II] 205 μm line (1461.13 GHz; hereafter [N II]), one can use the steep dependence of the [N II] to CO(7−6) flux ratio on $C(60/100)$ to estimate $C(60/100)$ or T_{dust}, with an accuracy equivalent to ~2 K in T_{dust} if the dust emissivity power-law index β is around 2 (Lu15). $C(60/100)$ is empirically related to

Σ_{SFR}, the average SFR surface density (Liu et al. 2015; Lutz et al. 2016), another fundamental parameter of galaxy SF. This indirect estimate of Σ_{SFR} is useful at high z, where it is often challenging to spatially resolve a galaxy. This dual-line strategy also allows for estimating additional galaxy physical parameters, including the SF area ($\approx$SFR/Σ_{SFR}), the molecular gas mass (M_{gas}) from the continuum flux underlying the CO(7−6) line (Scoville et al. 2016), and the gas depletion time τ_{gas} ($=M_{gas}$/SFR). If the lines are sufficiently resolved spectrally and spatially, insights into the gas dynamics can also be gained.

In a Cycle-3 program with the Atacama Large Millimeter/submillimeter Array (ALMA), we conducted a spectral line snapshot survey of eight ULIRGs and four LIRGs of $4 < z \lesssim 5.5$ to complete their detections in [N II] and CO(7−6). All our targets have prior detections in the [C II] 158 μm line (hereafter [C II]). In this Letter, we present the results from our [N II] observation of the interacting galaxy group BRI 1202-0725 at $z = 4.7$ (Isaak et al. 1994). This un-lensed system consists of two ULIRGs: a QSO at $z = 4.695$ and an optically obscured, submillimeter galaxy (SMG) at $z = 4''.692$ and $3''.8$ (~25 kpc) northwest of the QSO (Hu et al. 1996; Ohta et al. 1996; Omont et al. 1996; Yun et al. 2000;
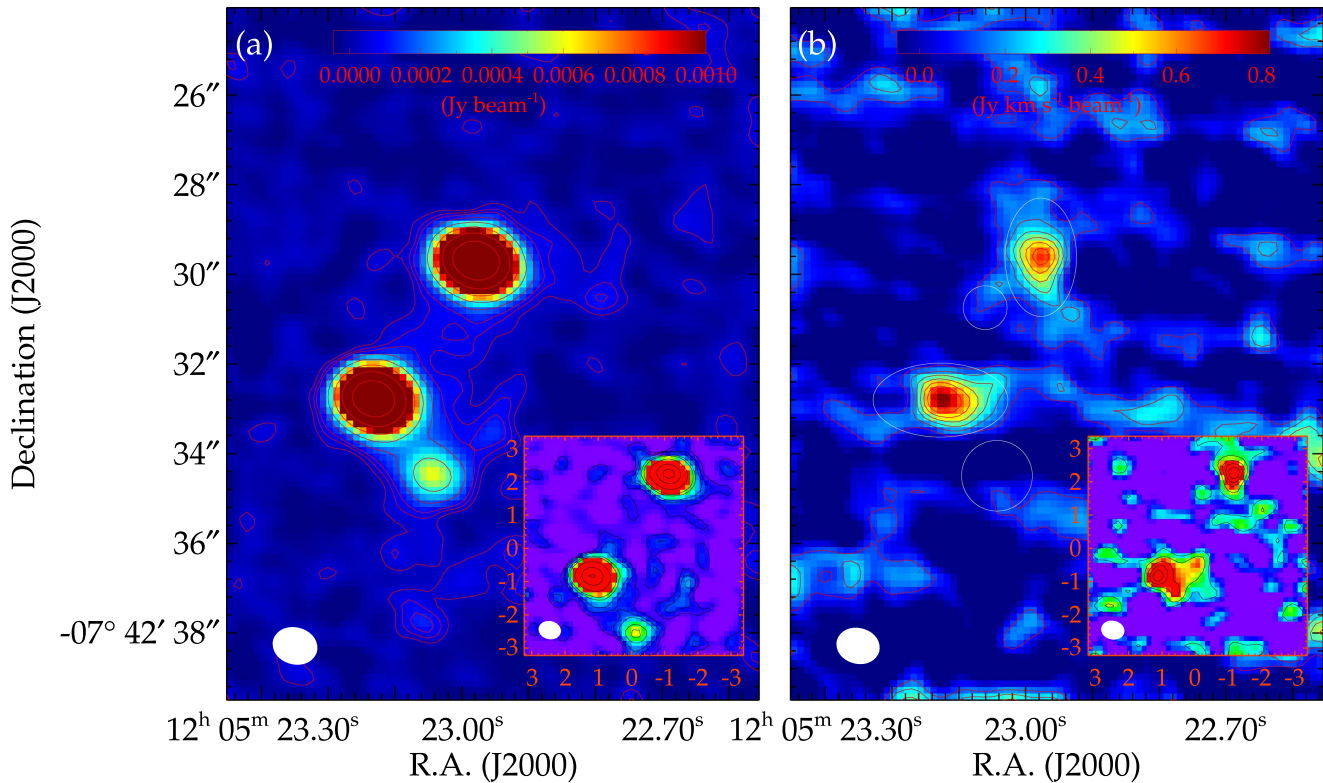
Figure 1. Images of (a) the continuum in Jy beam^{-1} and (b) [N II] in Jy km s^{-1} beam^{-1}, using the data cleaned with the natural weighting. The effective beam ($1''0 \times 0''8$, PA = 75°) is shown near the bottom left corner. The [N II] image was integrated over ν_{obs} = 256.148–257.090 GHz. Both image and contours refer to the same emission. The continuum and [N II] contours are at (1, 2, 3, 6, 12, 24, 48, 96, 147, 176.5) × 34 μJy beam^{-1} (=1σ) and (1, 2, 3, 4, 5, 7) × 0.104 Jy km s^{-1} beam^{-1} (=1σ), respectively. The four white ellipses in the [N II] image mark the apertures used to extract the 1d spectra. The smallest ellipse is centered on LAE1. The insert in each panel shows a $6''75 \times 6''75$ section, centered at (12^{h}05^{m}23^{s}05, −7°42′31″85), of the same image, but based on the data cleaned with the Briggs weighting (with *robust* = 0) that produced a finer effective beam of $\sim0''7 \times 0''6$ (as plotted). Here, the contours are at (1, 2, 3, 6.3, 9.4, 25, 62.5, 104) × 48 μJy beam^{-1} (=1σ) and (1, 2, 3, 3.9, 4.7) × 0.117 Jy km s^{-1} beam^{-1} (=1σ) for the continuum and [N II] images, respectively.

Carilli et al. 2002; Yun & Carilli 2002; Momjian et al. 2005; Iono et al. 2006; Salomé et al. 2012). In addition, two Lyα emitting galaxies (LAEs) have been detected in this system, with the first one (LAE1) located between the QSO and SMG, at $\sim2''3$ northwest of the QSO and the second one (LAE2) at $2''7$ southwest of the QSO (Fontana et al. 1996; Hu et al. 1996; Ohta et al. 2000; Ohyama et al. 2004).

The [C II] emission was detected with ALMA on all the member galaxies, along with a possible extended gas ridge between the QSO and SMG (Wagg et al. 2012; Carilli et al. 2013). Both QSO and SMG were also detected in CO(7−6) and CO(5−4) (Omont et al. 1996; Salomé et al. 2012). Decarli et al. (2014) presented the [N II] spectra of the system obtained with the IRAM interferometer and suggested possible [N II] detections for the SMG and LAEs, but a non-detection for the QSO. However, the [N II] line peak flux densities of both QSO and SMG (see Figure 2) are either near or below the spectral noise in Decarli et al. This might explain the flux discrepancy between ours and theirs. Pavesi et al. (2016) analyzed an archival ALMA observation and derived the [N II] fluxes of 0.74 (±0.07), 1.5 (±0.2), and 0.30 (±0.06) Jy km s^{-1} for the QSO, SMG, and LAE2, respectively, and a 3σ flux density upper limit of 0.5 mJy for LAE1.

The [N II] line is a major cooling line for ionized gas in galaxies. This line has only been detected in a handful of galaxies at $z \gtrsim 4$ (e.g., Combes et al. 2012; Decarli et al. 2012; Nagao et al. 2012; Rawle et al. 2014; Béthermin et al. 2016;

Pavesi et al. 2016). Our ALMA [N II] observation of BRI 1202-0725 detected both SMG and QSO at good S/N. In Section 2, we describe our observations and results. In Section 3, we analyze the observed [N II] and dust continuum emissions, and discuss the SF properties and [N II]/[C II] flux ratios of the galaxies in BRI 1202-0725. We use a flat cosmology with $\Omega_M = 0.27$, $\Omega_\Lambda = 0.73$, and $H_0 = 71$ km s^{-1} Mpc^{-1}. At $z = 4.694$, the luminosity distance is 44,172 Mpc, and 1″ corresponds to 6.6 kpc.

2. Observations and Results

BRI 1202-0725 was observed in ALMA Band 6 in the time division mode. Of the four spectral windows (SPWs), each of 1875 MHz wide, one was targeted at the redshifted [N II] line (at ~256.6 GHz) and the other three, centered at 254.6, 240.6, and 238.6 GHz, respectively, were used for continuum measurements. Each SPW has 128 channels with an effective resolution of 31.25 MHz (~36.5 km s^{-1}). The observation consisted of two independent executions, each with a 20.3 minute on-target integration. The first was executed on 2016 January 8 using 37 antennas covering baselines from 15.1 to 310.2 m and the second on 2016 March 13 using 38 antennas and baselines ranging from 15.1 to 460.0 m. The phase, bandpass, and flux calibrations were based on the quasars J1229+0230 and J1159−0940. The data reduction was carried out with the Common Astronomy Software Applications 4.5.3, and the final images were cleaned using the natural weighting,

Table 1
BRI 1202-0725: Observed and Derived Parameters[a]

Parameter	Unit	QSO	SMG	LAE2	LAE1
Continuum:					
R.A.[b]	J2000	$12^h05^m23\overset{s}{.}13$	$12^h05^m22\overset{s}{.}98$	$12^h05^m23\overset{s}{.}04$	...
Decl.[b]	J2000	$-7°42'32\overset{''}{.}8$	$-7°42'29\overset{''}{.}7$	$-7°42'34\overset{''}{.}5$	...
S_ν(256 GHz)[c]	mJy	7.58 ($\pm$0.01)	7.20 ($\pm$0.01)	0.83 $\pm$ 0.01	<0.10
Gaussian fit[c]	...	($1\overset{''}{.}08 \times 0\overset{''}{.}89$, 73°)	($1\overset{''}{.}08 \times 0\overset{''}{.}87$, 75°)	($1\overset{''}{.}20 \times 0\overset{''}{.}98$, 122°)	...
[N II]:					
Aperture[d]	...	($3'' \times 1\overset{''}{.}65$, 90°)	($2\overset{''}{.}65 \times 1\overset{''}{.}6$, 0°)	($1\overset{''}{.}6 \times 1\overset{''}{.}6$, 0°)	($1'' \times 1''$, 0°)
z[e]	...	4.695	4.693	...	...
Flux[f]	Jy km s^{-1}	1.01 ($\pm$0.02)	0.99 ($\pm$0.02)	<0.13	<0.02
FWHM[g]	km s^{-1}	380	794	...	...
Diameter[h]	kpc	9	14	...	...
Derived parameters:					
$L_{CO(7-6)}$[i]	$10^8 L_\odot$	6.6 ($\pm$0.6)	8.9 ($\pm$1.2)	...	...
$L_{[C\ II]}$[j]	$10^9 L_\odot$	6.5 ($\pm$1.0)	10.0 ($\pm$1.5)	...	...
$L_{[N\ II]}$	$10^8 L_\odot$	5.3 ($\pm$0.1)	5.2 ($\pm$0.1)	...	...
T_{dust}[k]	K	43 ($\pm$2)	43 ($\pm$2)	...	...
L_{FIR}[l]	$10^{13} L_\odot$	2.3 ($\pm$18%)	2.4 ($\pm$18%)	...	...
L_{IR}[m]	$10^{13} L_\odot$	5.0 ($\pm$30%)	6.7 ($\pm$30%)	...	...
SFR[m]	$10^3 M_\odot$ yr^{-1}	5.1 ($\pm$30%)	6.9 ($\pm$30%)	...	...
Σ_{SFR}[n]	$10^2 M_\odot$ yr^{-1} kpc^{-2}	16/21	18/21	...	...
SF diameter[o]	kpc	1.3	1.5	...	...
M_{H_2}[p]	$10^{11} M_\odot$	5	5	...	...
τ_{gas}[q]	10^7 years	10	7	...	...

Notes.

[a] All SFRs are consistent with Equation (4) in Kennicutt (1998), but scaled to Chabrier IMF. The ALMA flux uncertainties cited do not include the absolute calibration uncertainty.

[b] From the Gaussian fit.

[c] Continuum flux density from the Gaussian fit of which the major and minor FWHM axes and the major axis PA are given. The 3σ flux upper limit for LAE1 assumes an unresolved case.

[d] Aperture for the 1d spectrum extraction: major $\times$ minor axes, followed by the major axis PA.

[e] Redshift (in LSR) from the peak frequency of the Gaussian spectral line fit.

[f] Flux from the Gaussian line fit. The upper limit for LAE2 was derived using a Gaussian profile with a peak flux density of 3σ and a FWHM equal to that of the [C II] emission in Carilli et al. (2013). For LAE1, which has a narrow line width, this is simply 3σ times 100 km s^{-1}. Here, σ is the channel-to-channel noise in the spectrum in Figure 2.

[g] FWHM of the Gaussian line fit.

[h] Major axis of the Gaussian fit to the [N II] image in Figure 1, after deconvolution with the ALMA beam.

[i] Based on the line fluxes in Salomé et al. (2012).

[j] Based on the line fluxes in Wagg et al. (2012).

[k] Adopted dust temperature.

[l] The 42–122 μm luminosity from the FIR dust SED fit. The uncertainty corresponds to a variation of ± 2 K in T_{dust}.

[m] Inferred from $L_{CO(7-6)}$.

[n] Two estimates on Σ_{SFR}: the first one from $C(60/100)$ (Liu et al. 2015) and the second one from the 70-to-160 μm color of the SED fit (Lutz et al. 2016).

[o] FWHM of the SF region, assuming $\Sigma_{SFR} = 2000\ M_\odot$ yr^{-1} kpc^{-2}.

[p] Molecular gas mass inferred from the rest-frame 850 μm luminosity of the SED fit.

[q] Gas depletion time.

resulting in a synthesized beam of $1\overset{''}{.}0 \times 0\overset{''}{.}8$ (FWHM) at a position angle (PA) of 75° (N to E) for both continuum and line data. The rms noise in the continuum image, which is the average of the 3 continuum SPWs, is $\sim 34\ \mu$Jy beam^{-1}. The final [N II] spectral cube has a velocity channel width of 100 km s^{-1}, with an rms noise of ~ 0.3 mJy beam^{-1} in individual channels.

We compare in Figure 1 the continuum image and the [N II] image integrated over $\nu_{obs} = 256.148$–257.090 GHz, which encompasses all and the vast majority of the [N II] fluxes from QSO and SMG, respectively. While the QSO, SMG, and LAE2 are all detected in the continuum, only the QSO and SMG are clearly detected in [N II]. There appears to exist some faint (up to 3σ or 0.1 mJy beam^{-1}) dust emission connecting the QSO

and SMG, with a morphology similar to what is seen in [C II] (Carilli et al. 2013). However, its counterpart is not detected in the [N II] image. The outer [N II] emission contours (up to 3σ levels) of both QSO and SMG show distortions. To gain a better insight into this, we also cleaned the data using the Briggs weighting (with *robust* = 0) to lower the sidelobes and to effectively enhance the resolution to $0\overset{''}{.}7 \times 0\overset{''}{.}6$ (PA ≈ 78°). The results are shown in the insert in each panel in Figure 1 for an image section covering our targets. While the [N II] emission of the SMG remains in a similar morphology, that of the QSO is marginally resolved into three peaks: (i) the brightest one aligns with the peak dust emission; (ii) the second one ($12^h05^m23\overset{s}{.}09$, $-7°42'33\overset{''}{.}2$) is $\sim 0\overset{''}{.}7$ southwest of (i), in the direction of LAE2; (iii) the third one ($12^h05^m23\overset{s}{.}06$, $-7°42'32\overset{''}{.}5$) is $\sim 1''$
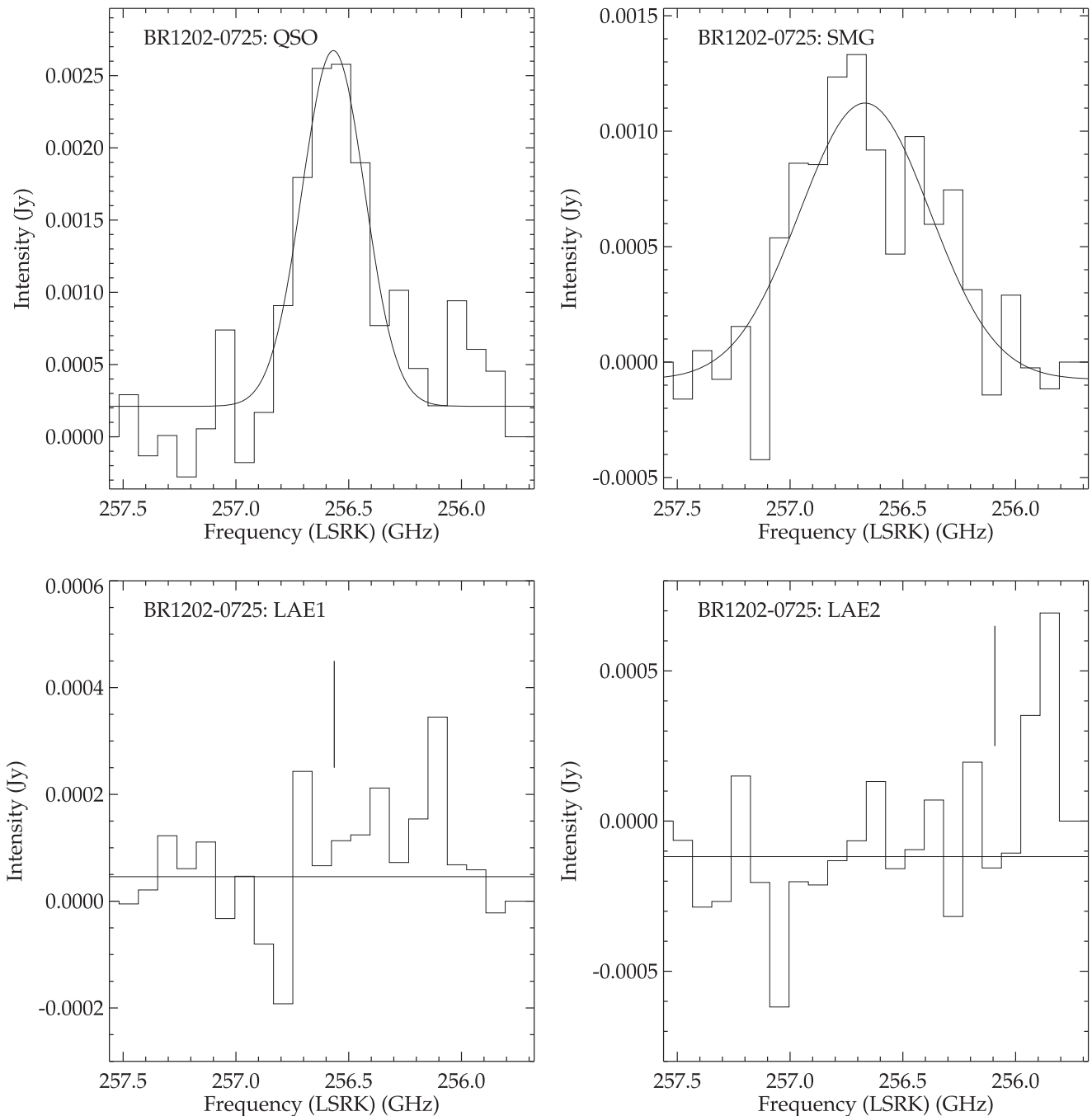
Figure 2. Individual spectra extracted using the elliptical apertures shown in Figure 1, plotted as a function of the observed frequency. Each frequency bin corresponds to 100 km s^{-1}. The Gaussian fits are also plotted for both QSO and SMG. The vertical bar in the spectra of LAE1 and LAE2 indicates the [N II] peak frequency expected from the redshift of the [C II] line observed in Carilli et al. (2013).

northwest of (i), with a peak surface brightness just under 3σ. While (i) and (iii) have similar line central velocities, (ii) is blueshifted by $\sim$200 km s^{-1} relative to (i). Contributing to $\sim$10% of the total [N II] flux of the QSO, (iii) is the main cause of the distorted contours seen. The relative positions of (ii) and (iii) are suggestive of tidal interaction or gas connection between the member galaxies.

3. Analysis and Discussion

In this section, we analyze the [N II] and continuum emissions and derive the parameters in Table 1 using the data cleaned with the natural weighting.

3.1. [N II] Line Emission

In Figure 2, we show the [N II] spectra extracted within the elliptical apertures defined in Table 1. For the QSO and SMG, we fit to their spectrum a single Gaussian profile plus a constant to derive the line flux. The resulting [N II] line widths are similar to or slightly wider than those of the corresponding CO and [C II] lines (Salomé et al. 2012; Carilli et al. 2013). For the LAEs, the frequency location of the [N II] peak emission is marked in Figure 2, based on the [C II] redshift (Carilli et al. 2013). Neither LAE is detected here.

Both SMG and QSO are spatially resolved in our [N II] image. A 2d Gaussian fit to the [N II] image of the SMG
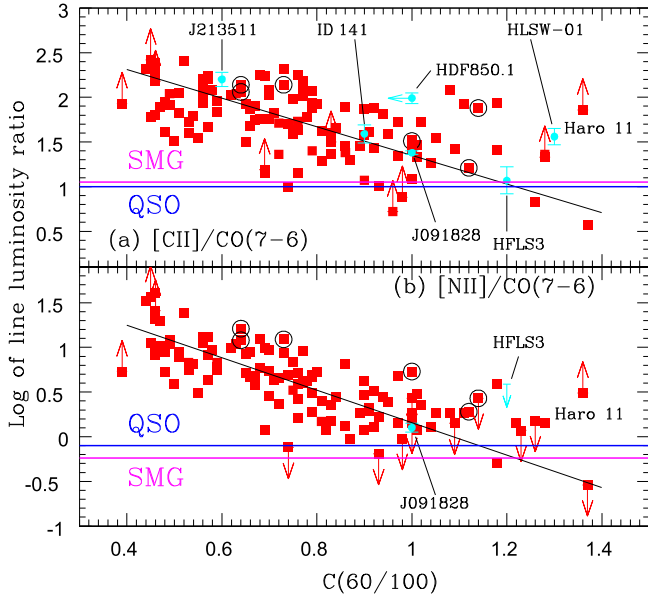
Figure 3. Comparisons of the QSO (blue line) and SMG (magenta line) in BRI 1202-0725 with (i) the local (U)LIRGs (red squares) and (ii) high-z galaxies from Lu15 in plots of (a) the logarithmic [C II] to CO(7−6) luminosity ratio and (b) the logarithmic [N II] to CO(7−6) luminosity ratio, as functions of the FIR color. The black solid line in each plot is a least-squares bisector fit to the detections of the local (U)LIRGs, except for the six dominant AGNs (further circled; see Lu15). For the [N II] line, this fit is given in Equation (6) in Lu15; for the [C II] line, this fit is log [C II]/CO(7−6) = $(-1.61 \pm 0.12)C(60/100) + (2.95 \pm 0.09)$.

(Figure 1(b)) yielded $2.''3 \times 1.''1$ (FWHM along each axis), with the major axis at PA $\approx 12°$. For the QSO, these values are $(1.''6 \times 0.''9, \mathrm{PA} \approx 91°)$. After a deconvolution with the ALMA beam, they become $(2.''1 \times 0.''5, \mathrm{PA} \approx 10°)$ and $(1.''3 \times 0.''4, \mathrm{PA} \approx 95°)$ for the SMG and QSO, respectively. The de-convolved major axes correspond to ~ 14 and 9 kpc for the SMG and QSO, respectively. Both QSO and SMG are unresolved in the continuum (see Section 3.2) and also appear to be unresolved in [C II] in Carilli et al. (2013) beam size $1.''2 \times 0.''8$). Therefore, the [N II] emission is much more extended (or diffuse) than the dust or [C II] emission in these galaxies.

For the QSO, the [N II] channel images reveal that the most blueshifted (redshifted) emission is located at the southwestern (northeastern) side of the galaxy, consistent with a rotation. For the SMG, the [N II] channel images do not support a position–velocity pattern consistent with a rotation. These are all consistent with what is seen in CO(5−4) and [C II] (Salomé et al. 2012; Carilli et al. 2013).

3.2. Dust Continuum

We derive the total continuum flux density of a galaxy by fitting a 2d Gaussian to the galaxy image in Figure 1(a) after temporarily masking out the other galaxies. The resulting Gaussian FWHMs (in Table 1) confirm that both QSO and SMG are unresolved. (In fact, the insert in Figure 1(a) shows that, even at the enhanced resolution of $\sim 0.''7$, they are still unresolved with the following fitted Gaussian FWHMs: $0.''73 \times 0.''59$ (PA = 76°) for the QSO and $0.''75 \times 0.''58$ (PA = 89°) for the SMG.) Table 1 shows that LAE2 is largely resolved.

In Figure 3, we plot the [C II]/CO(7−6) and [N II]/CO(7−6) flux ratios, each as a function of $C(60/100)$, for the local (U)
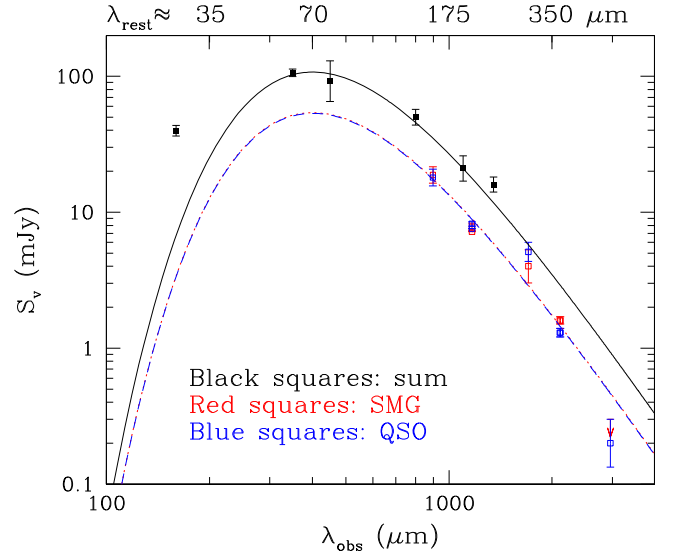

Figure 4. Plot of the continuum measurements (squares) and model SED fits (dashed curves) as a function of λ_{obs} for the QSO (in blue) and SMG (red). The measurements applicable only to the two galaxies combined are shown in black, so is the sum of the individual SED fits. Each SED fit fixed $\beta = 1.8$ and $T_{\mathrm{dust}} = 43$ K. The data points in color are at $\lambda_{\mathrm{obs}} = 2961 \ \mu m$, 2110 μm, 1705 μm (Salomé et al. 2012), 1167 μm (this work and Decarli et al. 2014) and 898 μm (Wagg et al. 2012), respectively. The black data points are at $\lambda_{\mathrm{obs}} = 1350 \ \mu m$ (Omont et al. 1996), 1100 μm, 800 μm, 450 μm (Isaak et al. 1994), 350 μm (Benford et al. 1999), and 160 μm (Leipski et al. 2010), respectively.

LIRGs and high-z galaxies used in Lu15. The corresponding flux ratios of the QSO and SMG in BRI 1202-0725 are indicated by the horizontal lines. The black line in each plot is a least-squares bisector fit (Isobe et al. 1990) to the local (U)LIRGs of detections only, excluding the AGNs (see Figure 3 caption). For the SMG, the corresponding line flux ratio intercepts the black line at $C(60/100) \approx 1.19$ in (a) and ≈ 1.23 in (b). The difference between these values is smaller than the scatter (0.15–0.2) in these plots. We therefore simply adopt their average value of 1.21. For the QSO, such determined $C(60/100)$ values are 1.22 and 1.15, respectively. Even though there is some apparent segregation between the AGNs and the rest of the local (U)LIRGs in Figure 3(b), the AGN sample size is still too small to draw a firm conclusion on this. We therefore also adopt the average $C(60/100) = 1.19$ for the QSO. We set the uncertainty of these FIR colors to the horizontal scatter w.r. t. the black line in the [N II] plot, i.e., ~ 0.15. Assuming $\beta = 1.8$ (Planck Collaboration et al. 2011), these adopted FIR colors correspond to $T_{\mathrm{dust}} \approx 43 \ (\pm 2)$K.

The QSO and SMG are only spatially separated by a few existing interferometric observations, all at the long-wavelength side of their SED peak (see Figure 4). The T_{dust} determined above provides a crucial constraint on the SED shape. Our best modified-blackbody SED fits for the QSO and SMG separately, after fixing T_{dust} at 43 K and β at 1.8, are also shown in Figure 4. We note that similar SED fits would be obtained by using only the continuum flux from the CO(7−6) observation and our adopted $C(60/100)$. The luminosity of the SED fit integrated over 20–1000 μm is 2.9 (3.0) $\times 10^{13} L_\odot$ for the QSO (SMG). These values are 3–5 times larger than those in Salomé et al. (2012). The L_{FIR} (over 42−122 μm) from our SED fit is 2.3 (2.4) $\times 10^{13} L_\odot$, resulting in a log $L_{\mathrm{CO(7−6)}}/L_{\mathrm{FIR}} \approx -4.54 \ (-4.42)$ for the QSO (SMG). These values agree with the average of -4.61 for our local

(U)LIRG sample to within $\sim 1.5\sigma$, where σ (≈ 0.12) is the local sample standard deviation (see Lu15).

3.3. Star Formation Properties

Following Lu15, the SFR inferred from $L_{CO(7-6)}$ is 5.1 (6.9) $\times 10^3 \, M_\odot \, \mathrm{yr}^{-1}$ for the QSO (SMG) using the initial mass function (IMF) of Chabrier (2003). For local (U)LIRGs, Σ_{SFR} is empirically correlated with $C(60/100)$ (Liu et al. 2015) or T_{dust} (Lutz et al. 2016). The scatter of these correlations is fairly significant, e.g., ~ 0.6 dex in Lutz et al. (2016). Nevertheless, these two independent correlations give comparable estimates for Σ_{SFR}: $\sim 2 \times 10^3 \, M_\odot \, \mathrm{yr}^{-1} \, \mathrm{kpc}^{-2}$ for both QSO and SMG after we adjusted their correlations to Chabrier IMF and increased the L_{FIR}-based SFR in Lutz et al. by a factor of 2 to align with the Kennicutt (1998) formula. These estimates of Σ_{SFR} are quite high, but still below the Eddington limit of $\sim 3 \times 10^3 \, M_\odot \, \mathrm{yr}^{-1} \, \mathrm{kpc}^{-2}$ (Murray et al. 2005; Thompson et al. 2005; Hopkins et al. 2010). The face-on FWHM diameter, d, of the SF region can be estimated via $\Sigma_{SFR} = \left(\frac{1}{2} \, \mathrm{SFR}\right) / \left(\frac{1}{4}\pi \, d^2\right)$. For $\Sigma_{SFR} = 2 \times 10^3 \, M_\odot \, \mathrm{yr}^{-1} \, \mathrm{kpc}^{-2}$, the resulting $d = 1.3$ (1.5) kpc for the QSO (SMG), consistent with them being unresolved in our continuum image. These sizes are somewhat smaller than the ~ 2 kpc scale resolved in a high-resolution CO(2−1) image (Carilli et al. 2002), a phenomenon that is also seen locally (Xu et al. 2014, 2015). Following Scoville et al. (2016), we estimated the molecular gas mass, M_{gas}, to be $5 \times 10^{11} \, M_\odot$ for either galaxy based on the rest-frame f_ν(850 μm) from our SED fit. The formal uncertainty for M_{gas} is about a factor of 2. The gas depletion time $\tau_{gas} \approx 10$ (7) $\times 10^7$ years for the QSO (SMG).

3.4. On [N II]/[C II] Ratios

For local (U)LIRGs, $\log L_{[N\,II]}/L_{[C\,II]}$ correlates linearly with $C(60/100)$, with a scatter of only ~ 0.15 in $\log L_{[N\,II]}/L_{[C\,II]}$ (Lu15). As $C(60/100)$ increases from 0.4 to ~ 1.3, $L_{[N\,II]}/L_{[C\,II]}$ drops by a factor of 4 (from 0.12 to 0.03). This correlation is due to an increasing contribution to [C II] from the neutral medium around young massive stars as $C(60/100)$ increases (see Díaz-Santos et al. 2017). Our observation shows that both QSO and SMG in BRI 1202-0725 follow this local trend as well.

Theoretical considerations predict a smaller [N II]/[C II] ratio for a lower metallicity (Nagao et al. 2012; Pareira-Santaella et al. 2017). In such a scenario, galaxies of different metallicities follow separate [N II]/[C II]−$C(60/100)$ tracks. In principle, one needs to know both [N II]/[C II] and $C(60/100)$ in order to constrain the metallicity of a galaxy. For example, our current observation sets [N II]/[C II] < 0.03 for the two LAEs. These limits alone are not stringent enough to conclude if the LAEs follow a different [N II]/[C II]−$C(60/100)$ track than the local (U)LIRGs.

References

Benford, D. J., Cox, P., Omont, A., et al. 1999, ApJL, 518, L65
Béthermin, De Breuck, C., Gullberg, B., et al. 2016, A&A, 586, L7
Carilli, C. L., Kohno, K., Kawabe, R., et al. 2002, AJ, 123, 1838
Carilli, C. L., Riechers, D., Walter, F., et al. 2013, ApJ, 763, 120
Chabrier, G. 2003, PASP, 115, 763
Combes, F., Rex, M., Rawle, T. D., et al. 2012, A&A, 538, L4
Decarli, R., Walter, F., Carilli, C., et al. 2014, ApJL, 782, L17
Decarli, R., Walter, F., Neri, R., et al. 2012, ApJ, 752, 2
Díaz-Santos, T., Armus, L., Charmandaris, V., et al. 2017, ApJ, submitted
Fontana, A., Cristiani, S., DOdorico, S., Giallongo, E., & Savaglio, S. 1996, MNRAS, 279, L27
Hopkins, P. F., Murray, N., Quataert, E., & Thompson, T. A. 2010, MNRAS, 401, L19
Hu, E. M., McMahon, R. G., & Egami, E. 1996, ApJL, 459, L53
Iono, D., Yun, M. S., Elvis, M., et al. 2006, ApJL, 645, L97
Isaak, K., McMahon, R. G., Hills, R. E., & Withington, S. 1994, MNRAS, 269, L28
Isobe, T., Feigelson, E. D., Akritas, M. G., & Babu, G. J. 1990, ApJ, 364, 104
Kennicutt, R. C., Jr. 1998, ARA&A, 36, 189
Leipski, C., Meisenheimer, K., Klaas, U., et al. 2010, A&A, 518, L34
Liu, L., Gao, Y., & Greve, T. R. 2015, ApJ, 805, 31
Lu, N., Zhao, Y., Díaz-Santos, T., et al. 2017, ApJS, 230, 1
Lu, N., Zhao, Y., Xu, C. K., et al. 2014, ApJL, 787, L23
Lu, N., Zhao, Y., Xu, C. K., et al. 2015, ApJL, 802, L11 (Lu15)
Lutz, D., Berta, S., Contursi, A., et al. 2016, A&A, 591, A136
Momjian, E., Carilli, C. L., & Petric, A. O. 2005, AJ, 129, 1809
Murray, N., Quataert, E., & Thompson, T. A. 2005, ApJ, 618, 569
Nagao, T., Maiolino, R., De Breuck, C., et al. 2012, A&A, 542, L34
Ohta, K., Matsumoto, T., Maihara, T., et al. 2000, PASJ, 52, 557
Ohta, K., Yamada, T., Nakanishi, K., et al. 1996, Natur, 382, 426
Ohyama, Y., Taniguchi, Y., & Shioya, Y. 2004, AJ, 128, 2704
Omont, A., Petitjean, P., Guilloteau, S., et al. 1996, Natur, 382, 428
Pareira-Santaella, M., Digopoulou, D., Frrah, D., et al. 2017, MNRAS, in press (arXiv:1705.0836)
Pavesi, R., Riechers, D. A., Capak, P. L., et al. 2016, ApJ, 832, 151
Planck Collaboration, Abergel, A., Ade, P. A. R., et al. 2011, A&A, 536, A25
Rawle, T. D., Egami, E., Bussmann, R. S., et al. 2014, ApJ, 783, 59
Salomé, P., Guélin, M., Downes, D., et al. 2012, A&A, 545, 57
Sanders, D. B., & Mirabel, I. F. 1996, ARA&A, 34, 749
Scoville, N., Sheth, L. K., Aussel, H., et al. 2016, ApJ, 820, 83
Thompson, T. A., Quataert, E., & Murray, N. 2005, ApJ, 630, 167
Wagg, J., Wiklind, T., Carilli, C. L., et al. 2012, ApJL, 752, L30
Xu, C. K., Cao, C., Lu, N., et al. 2014, ApJ, 787, 48
Xu, C. K., Cao, C., Lu, N., et al. 2015, ApJ, 799, 11
Yun, M. S., & Carilli, C. 2002, ApJ, 568, 88
Yun, M. S., Carilli, C. L., Kawabe, R., et al. 2000, ApJ, 528, 171